Traction open boundary condition for incompressible, turbulent, single- or multi-phase flows, and surface wave simulations

Cyril Bozonnet, Olivier Desjardins, Guillaume Balarac

Traction open boundary condition for incompressible, turbulent, single- or multi-phase flows, and surface wave simulations

Cyril Bozonnet[a,b,*], Olivier Desjardins[b], Guillaume Balarac[a,c]

[a] *Univ. Grenoble Alpes, CNRS, Grenoble INP, LEGI, 38000 Grenoble, France*
[b] *Sibley School of Mechanical and Aerospace Engineering, Cornell University, Ithaca, NY 14853, USA*
[c] *Institut Universitaire de France (IUF)*

Abstract

In simulations, artificial boundaries need to be introduced to limit the size of computational domains and thereby lower computational cost. At these boundaries, flow variables need to be calculated in a way that will not induce any perturbation of the interior solution, which poses a great challenge in incompressible flows. In this paper, we demonstrate the potential of a new traction open boundary condition to address the classical problems encountered in simulations with open boundary conditions: backflow instability, wave reflections, and confinement caused by the proximity of the outlet. This novel boundary treatment, based on a Lagrangian estimation of the traction in the outlet section coupled to a stabilization term, is shown to provide accuracy and stability for turbulent, single- or multi-phase flows, test cases. Using a simulation of surface gravity waves, we show that if special care is given to the computation of the estimated traction, it is possible to get a fully non-reflective open boundary condition.

Keywords: Outflow, non-reflective boundary, backflow instability

1. Introduction

Due to the finite nature of numerical simulations, it is often necessary to truncate computational domains. This requires imposing artificial boundaries along with the associated mathematical conditions that close the system of equations to be solved. The primary goal of such boundaries is to restrict

the computation to a given region of interest without perturbing the solution inside the domain, thereby limiting cost. In the case of outflow boundaries, the flow should be allowed to leave the computational domain in the most natural way possible without undergoing any perturbations that could propagate upstream and thus pollute the upstream solution. Moreover, complex dynamics may occur at the artificial boundary and the flow may contain regions of both outflow and backflow, i.e., regions of flow reversal where the outlet boundary acts as an inlet, potentially polluting the solution [1].

The definition of an ideal open boundary condition (OBC) for incompressible fluid dynamic simulations is still an unresolved topic, as demonstrated by Sani and Gresho after the "Open boundary condition minisymposium" [2], or by other authors in recent reviews [1, 3]. However, one can describe the effect of a non-ideal OBC on a simulation result. In wave-like simulations, the phenomena of wave reflection can create unrealistic flows, instabilities and prevent the flow from reaching a statistical equilibrium over a long computational time [4]. In turbulent flows, the presence of backflow can cause the system to experience an uncontrolled growth in kinetic energy, which has for example been evidenced in biofluids simulations [5].

More generally, the choice of OBC can severely influence the size of the computational domain due to the difficulty of finding a condition that does not durably affect the upstream flow, the most famous example being the impact of the outflow position on a cylinder drag and lift coefficients [6]. Indeed, the incompressibility constraint and the unphysical nature of domain truncations may prevent finding a perfect OBC. However, in this paper, we endeavor to present a novel boundary treatment that reduces the error induced by outlet position on severely truncated domains and is stable to backflow, in addition to satisfying the incompressibility constraint.

In the next section, the main types of outflow treatments are discussed. The new proposed strategy is then presented. In section 3, the numerical implementations of these boundary conditions are presented in the context of a fractional step method with pressure projection method. Section 4 is devoted to single phase test cases, consisting of the Kovasznay flow for measuring spatial convergence, a time-dependent manufactured solution test for measuring temporal convergence, and a flow past a square and a turbulent plane jet to explore the stability and accuracy of the method. Finally, multiphase test cases are considered in section 5, with the convection of a high density droplet, a turbulent swirling liquid jet, and the transport of surface gravity waves. All of the work presented hereafter is applied to outlet boundary con-

ditions where the flow is expected to be mostly leaving the computational domain, but it can be applied as well on lateral and inlet boundaries.

2. Existing methods and present work

Before giving a short review of existing methods we introduce here some useful notations. The computational domain will be refered to as Ω. This domain is bounded by real and artifical (open) boundaries. The firsts ones are denoted $\partial\Omega_d$ and the laters $\partial\Omega_o$. $\partial\Omega$ will refer to both types of boundaries, i.e., $\partial\Omega = \partial\Omega_d \cup \partial\Omega_o$. The vector $\mathbf{n}$ is defined as the unit normal to those boundaries, always oriented toward the exterior of the domain.

2.1. Existing methods

Apart from classical Dirichlet and Neumann conditions, one of the most widely used boundary conditions is the convective boundary condition,

$$\frac{\partial \phi}{\partial t} + c\frac{\partial \phi}{\partial n} = 0. \tag{1}$$

This equation represents the transport of a quantity ϕ through a boundary of normal $\mathbf{n}$ with a phase speed c, where n is the coordinate in the $\mathbf{n}$ direction. This condition, known as the Sommerfeld equation, or the radiation condition, is in fact an exact absorbing condition, i.e., specification of the incoming characteristic to zero, for a 1D wave equation with a constant wave speed [1]. The most famous choice of phase speed comes from the work of Orlanski [7]: c is computed locally based on known values of ϕ in the vicinity of the boundary. This solution has been shown to result in a phase velocity close to white noise [8]. Despite some improvements of Orlanski's method [9], it seems that no satisfying method has emerged to obtain an accurate estimation of the phase velocity without *a priori* knowledge of it [1, 10].

A general mathematical approach to obtain exact absorbing boundary conditions has been derived [11]. However, to our knowledge, no applications of this method to Navier-Stokes equations have been presented, the closest being recent progress on shallow-water equations [1]. It has been applied to a 2D wave equation whose coefficients are then identified using the Navier-Stokes equations [12]. It results in a condition similar to Eq. (1) with the phase velocity evaluated as the local speed and the presence of a viscous term on the right hand side. More generally, a whole family of OBCs relies on the method of characteristics [1].

On the other hand, another type of boundary condition can be directly derived from the Navier-Stokes equation in its weak form [13]: the traction boundary condition. It consists of applying a condition on the normal stress at the artificial boundary,

$$\overline{\overline{\sigma}} \cdot \mathbf{n} = (-p\mathbf{I} + \mu(\nabla \mathbf{u} + \nabla \mathbf{u}^T)) \cdot \mathbf{n} = \mathbf{t}, \tag{2}$$

where $\overline{\overline{\sigma}}$, p, μ and $\mathbf{u}$ are the stress tensor, the pressure, the dynamic viscosity, and the velocity, respectively. $\mathbf{t}$ is a traction vector that must be prescribed. No clear guidelines exist for the choice of this vector. The most widespread choice is $\mathbf{t} = \mathbf{0}$, giving the well-known "traction-free" boundary condition [14, 15]. The traction $\mathbf{t}$ has also been computed locally and iteratively [13], based on previous runs on longer domains [2], or defined analytically with a Stokes solution [16].

As stated previously, the presence of backflow at an outlet boundary could lead to an instability due to an uncontrolled growth of kinetic energy. To understand it, the energy balance in the overall computational domain, Ω, can be considered [17, 18],

$$\begin{aligned} \frac{\partial}{\partial t} \int_\Omega \frac{1}{2} \rho |\mathbf{u}|^2 = &- \int_\Omega \frac{\mu}{2} \|\mathbf{D}(\mathbf{u})\|^2 + \int_\Omega (\rho \mathbf{g} + \mathbf{T}_\sigma) \cdot \mathbf{u} \\ &+ \int_{\partial\Omega_d} \left(\overline{\overline{\sigma}} \cdot \mathbf{n} - \frac{1}{2} \rho |\mathbf{u}|^2 \mathbf{n} \right) \cdot \mathbf{u} \\ &+ \int_{\partial\Omega_o} \left(\overline{\overline{\sigma}} \cdot \mathbf{n} - \frac{1}{2} \rho |\mathbf{u}|^2 \mathbf{n} \right) \cdot \mathbf{u}, \end{aligned} \tag{3}$$

Where ρ is the density, $\mathbf{g}$ is the gravity vector, $\mathbf{D}(\mathbf{u})$ is the shear rate tensor and $\mathbf{T}_\sigma$ represents surface tension forces. It results that the rate of change of kinetic energy is controlled by viscous dissipation (exchange with internal energy), gravity (exchange with potential energy), surface tension (exchange with surface energy) and by two surface terms. The first one is expressed on $\partial\Omega_d$, the Dirichlet boundaries, where variables are known. The second surface term is expressed on $\partial\Omega_o$, the outflow boundary, where all variables have to be computed. In case of backflow, the convective part of this term becomes positive and can lead to a global increase of kinetic energy, leading to the instability of the system.

Following Eq. (3), one possible backflow treatment is to ensure that the last term is zero, preventing backflow from causing an unstable growth of

kinetic energy. It leads to the following OBC

$$\overline{\overline{\sigma}} \cdot \mathbf{n} = (-p\mathbf{I} + \mu(\nabla \mathbf{u} + \nabla \mathbf{u}^T)) \cdot \mathbf{n} = \frac{\rho}{2} f(\mathbf{u})\mathbf{n}, \tag{4}$$

with $f(\mathbf{u})$ chosen so that it cancels the last term of Eq. (3) in case of backflow, for example

$$f(\mathbf{u}) = \begin{cases} (\mathbf{u} \cdot \mathbf{n})^2 & \text{if } \mathbf{u} \cdot \mathbf{n} < 0, \\ 0 & \text{otherwise.} \end{cases} \tag{5}$$

This condition is similar to the stabilized traction-free condition used for single phase flows [17, 19] and for multiphase flows [18, 20]. In case of backflow, the normal stress will compensate the normal influx of kinetic energy, whereas it will vanish in case of outflow. Different forms for $f(\mathbf{u})$ along with other types of backflow treatments have been reviewed [3].

The traction boundary condition, when used as the stabilized traction-free condition as in Eq. (4), requires the flow to be well-developped before reaching the boundary [13]. Several methods have already been proposed to combine stability and accuracy even at high Reynolds number, such as the "convective-like" traction boundary condition [21],

$$\overline{\overline{\sigma}} \cdot \mathbf{n} = -\mu D_0 \frac{\partial \mathbf{u}}{\partial t} + \frac{\rho}{2} \Theta(\mathbf{u} \cdot \mathbf{n})((\mathbf{u} \cdot \mathbf{n})\mathbf{u} + |\mathbf{u}|^2 \mathbf{n}), \tag{6}$$

where D_0 is computed using a characteristic velocity, and the function $\Theta(x)$ is essentially equal to 1 for negative value of x and 0 otherwise, see [21] for more details. The value of D_0 is found to have little effect on the overall flow, except on the flow patterns near the outlet boundary. An earlier method developped by Bruneau and Fabrie [16] combines a stabilization to backflow and a non-zero traction,

$$\overline{\overline{\sigma}} \cdot \mathbf{n} = \overline{\overline{\sigma}}^{ref} \cdot \mathbf{n} + \frac{\rho}{2} (\mathbf{u} \cdot \mathbf{n})^- (\mathbf{u} - \mathbf{u}^{ref}), \tag{7}$$

where the reference values are computed using an analytical solution, or evaluated from known values inside the domain [22], and $(\mathbf{u}\cdot\mathbf{n})^- = \max(0, -\mathbf{u}\cdot\mathbf{n})$. Note that this condition leads to a well-posed problem [23]. It has, to the best of our knowledge, not been applied to projection methods.

Another potential backflow treatment is to simply force all velocities such that $\mathbf{u} \cdot \mathbf{n} < 0$ to zero, thus preventing any influx of kinetic energy. This solution provides energy stability of the system, but we will show in section

5.1 that it can lead to severe inaccuracies in multiphase flows. In [4], when the phase velocity is computed as $\mathbf{u} \cdot \mathbf{n} < 0$, the use of external data allows to limit the occurence of the backflow instability.

As said in the introduction, the main difficulties encountered by outflow treatments are associated with the proper transmission of perturbations through the artificial boundary, and to the presence of inflow/backflow regions on it. One common way to overcome those issues is to try to dissipate, or damp, the fluctuating energy of the flow before the outlet using artificial zones called sponge layers or nudging layers. Sponge layers consist in the introduction of a dissipative source term in Navier-Stokes equations that becomes stronger when getting closer to the boundary [24]. Nudging layers consist of the relaxation of the flow towards prescribed external data [4]. These solutions are intentionally excluded from our study to focus on the improvements of an accurate OBC.

Finally, most efforts to get non-reflective and accurate boundaries have been focused on convective-like OBCs, often requiring the use of external data that is consistent with the backflow treatment [4], whereas traction boundary conditions present an easier way to deal with backflow without the need for external data. As said previously, the stabilized traction-free condition, Eq. (4), requires the flow to be well-developped before reaching the boundary [13]. Traction boundary conditions have, to our knowledge, never been applied to problems of wave reflections.

2.2. Generalized traction boundary condition

We propose a new traction boundary condition, inspired from the Bruneau and Fabrie condition Eq. (7), that combines the two following characteristics. Firstly, the flow will not be required to be well-developped at the boundary, which will be achieved by applying a non-zero traction at the boundary. Secondly, this OBC will be stable to influxes of kinetic energy due to backflow, which will be achieved by the inclusion of a stabilization term.

We express the traction at the boundary as

$$(-p\mathbf{I} + \mu(\nabla\mathbf{u} + \nabla\mathbf{u}^T)) \cdot \mathbf{n} = \mathbf{t}^{stab} + \alpha\mathbf{t}^{est}. \tag{8}$$

$\mathbf{t}^{stab}$ is a numerical treatment to ensure stability to backflow. $\mathbf{t}^{est}$ is an estimation of the traction at the outlet boundary and $\alpha = [0; 1]$ is an adjustable parameter. The accuracy of the present boundary treatment will depend on the choice of the last two terms.

Following Eq. (3), the stabilization term is taken such that it cancels the term responsible for the backflow instability in case of backflow,

$$\mathbf{t}^{stab} = \frac{\rho}{2} f(\mathbf{u})\mathbf{n}, \tag{9}$$

with $f(\mathbf{u})$ defined as in Eq. (5). Thus, the kinetic energy variation at the open boundary is not equal to zero, as with Eq. (4), but depends on the value of $\alpha\mathbf{t}^{est}$. The results presented in this paper show that this novel boundary condition is sufficient to ensure the stability of the system in the presence of backflow at the open boundary. If α is equal to zero, one can see that we recover the stabilized traction-free condition presented in [17].

To obtain the best possible traction estimate we introduce here the general idea behind our work. We propose $\mathbf{t}^{est}$, the estimated traction at the boundary, to be considered as a Lagrangian quantity. Its value can therefore be evaluated using an advection equation,

$$\frac{\partial \mathbf{t}^{est}}{\partial t} + \mathbf{u}_{ad} \cdot \nabla \mathbf{t}^{est} = \mathbf{0}, \tag{10}$$

where $\mathbf{u}_{ad}$ is an advection velocity that can be computed using an analytical expression, an averaged or a local velocity.

2.3. Scope of this work

The previous method to estimate the traction is very general and studying all possible ways to resolve it is beyond the scope of the present paper. Thus, we restrict our study to a few particular cases. We first assume a one dimensional advection velocity of the estimated traction in the outlet boundary normal direction. Then, we assume a first order explicit temporal resolution of Eq. (10) on a cartesian grid. The choice of an explicit resolution is a consequence of the algorithm used to solve the coupling between velocity and pressure, as we detail in the next section. Finally, we use a first order upwind discretization of the spatial term in order to use values inside the computational domain.

The traction estimation is therefore expressed as

$$\mathbf{t}^{est} = \left[\phi\overline{\overline{\sigma}}_{BC-1} \cdot \mathbf{n} + (1-\phi)\,\overline{\overline{\sigma}}_{BC} \cdot \mathbf{n}\right], \tag{11}$$

where the notations $BC-1$ and BC refer to the point just before the boundary and the boundary point, respectively. ϕ is an interpolation coefficient computed using numerical parameters and the one dimensional advection velocity. ϕ can be considered as a CFL condition and therefore has

here to be kept in the range $[0;1]$ as the advection is only done between the boundary point and its closest neighbour.

The previous choices of resolution for Eq. (10) are not suitable in case of discontinuities in the traction field. This latter point is limiting in case of multiphase flows due to the effect of surface tension. The presence of a pressure jump can thus deteriorate the traction estimation and create unphysical velocities, or even stability issues. Therefore, in case of multiphase flows we limit our study to high Weber number. A way to get around that difficulty would be to use, for example, a semi-Lagrangian advection method [25] for $\mathbf{t}^{est}$. Other aspects may have to be considered, such as the curvature computation in the vicinity of the open boundary, or the density boundary condition. Note that the use of multiphase traction-free condition in phase field method provides a natural way to get around that difficulty as a surface tension term appears in the outlet boundary energy flux [18].

For $\alpha = 0$, the generalized traction boundary condition, Eq. (8), reduces to

$$(-p\mathbf{I} + \mu(\nabla\mathbf{u} + \nabla\mathbf{u}^T)) \cdot \mathbf{n} = \frac{\rho}{2} f(\mathbf{u})\mathbf{n}, \tag{12}$$

which will be refered to as the stabilized traction-free condition (TF) in the following. TF is the same condition as used in [17]. For $\alpha = 1$ and $\phi = 1$, Eq. (8) reduces to

$$(-p\mathbf{I} + \mu(\nabla\mathbf{u} + \nabla\mathbf{u}^T)) \cdot \mathbf{n} = \frac{\rho}{2} f(\mathbf{u})\mathbf{n} + \overline{\overline{\sigma}}_{BC-1} \cdot \mathbf{n}, \tag{13}$$

which will be refered to as the estimated traction boundary condition (ET). This condition ressembles the Bruneau and Fabrie condition, Eq. (7). The choice $\phi = 1$ raises the question of the dependence of the accuracy to numerical parameters, as the traction at the point just before the boundary may not always be a good estimation. In the final part of the article, we will consider the $\phi \neq 1$ case, where Eq. (8) reduces to

$$(-p\mathbf{I} + \mu(\nabla\mathbf{u} + \nabla\mathbf{u}^T)) \cdot \mathbf{n} = \frac{\rho}{2} f(\mathbf{u})\mathbf{n} + \left[\phi\overline{\overline{\sigma}}_{BC-1} \cdot \mathbf{n} + (1-\phi)\,\overline{\overline{\sigma}}_{BC} \cdot \mathbf{n}\right], \tag{14}$$

which will be refered to as the convected traction boundary condition (CT). Note that in the previous three boundary conditions $f(\mathbf{u})$ is computed using Eq. (5).

In the rest of the paper we also use classic OBCs, such as the Neumann boundary condition (NM),

$$\frac{\partial \mathbf{u}}{\partial n} = 0, \tag{15}$$

or the convective boundary condition (CV),

$$\frac{\partial \mathbf{u}}{\partial t} + c\frac{\partial \mathbf{u}}{\partial n} = 0. \tag{16}$$

As mentioned previously the performance of such condition will be strongly linked to the choice of the convective velocity, which will be detailed later.

Finally, the main objectives of the present paper are, for each of the OBCs under consideration, to give a detailed description of the algorithm allowing to their use in the context of projection methods and VOF/Level Set methods, to demonstrate the importance of bakflow stabilization in single- or multiphase flows, and to demonstrate the stability and accuracy of the non-zero traction methods, such as ET or CT. CT will only be used in the end of the paper, where the level of accuracy obtained with ET is not satisfactory.

3. Mathematical formulation and algorithms

3.1. General framework

Fluid dynamics are governed by conservation laws, forming the Navier-Stokes system of equations. Conservation of mass is, providing that the flow is incompressible ($\nabla \cdot \mathbf{u} = 0$),

$$\frac{\partial \rho}{\partial t} + \nabla \cdot (\rho \mathbf{u}) = \frac{\partial \rho}{\partial t} + \mathbf{u} \cdot \nabla \rho = 0. \tag{17}$$

Multiphase momentum conservation is written in the framework of the one fluid formulation [26]: a single equation with space varying material properties is used to describe the dynamics of both phases. The effect of surface tension is added through a singular force, $\mathbf{T}_\sigma$, acting on the interface,

$$\frac{\partial \rho \mathbf{u}}{\partial t} + \nabla \cdot (\rho \mathbf{u}\mathbf{u}) = -\nabla p + \nabla \cdot \left(\mu \left[\nabla \mathbf{u} + \nabla \mathbf{u}^T\right]\right) + \mathbf{T}_\sigma + \rho \mathbf{g}. \tag{18}$$

In absence of phase change, the application of the momentum equation on the interface results in the classical jump condition for normal stress,

$$[p]_\Gamma = \sigma\kappa + 2\,[\mu]_\Gamma\, \mathbf{n}_\Gamma^T \cdot \nabla \mathbf{u} \cdot \mathbf{n}_\Gamma, \tag{19}$$

where σ, κ and $\mathbf{n}_\Gamma$ are the surface tension, the curvature and the normal vector to the interface Γ respectively. The notation $[.]_\Gamma$ represents the interfacial jump from liquid to gas.

These equations are solved using NGA, a finite volume, staggered-grid, second order flow solver [27]. Mass conservation, Eq. (17), is ensured through an unsplit semi-Lagrangian VOF advection method [25]. Momentum conservation, Eq. (18), is computed in a way consistent with mass transport and with the presence of interfacial discontinuities [28]. It is to be noted that all OBC methods presented are usable with any sharp interface-capturing method (VOF/Level-Set). For an application to diffuse interface methods, we refer the reader to a work for phase field method [18]. Interface boundary conditions, Eq. (19), are included in the pressure through the use of the ghost fluid method [29], with a curvature computed using a least-squares curve fitting method [30]. The coupling between velocity and pressure, required due to the incompressibility constraint, is enforced using an incremental pressure projection method [31]. In the following equations, superscripts n and $n+1$ refer to previous and new time steps, respectively, whereas subscript k refers to the subiterations of the iterative Crank-Nicolson time advancement scheme [32] used in the present solver. Note that we use an implicit resolution of the linearized problem at each subiteration, see [27] for more details. Second order centered schemes are used for spatial discretization on all terms but the convective term at the interface, where a consistent mass and momentum advection strategy is employed (see [28] for more details). In case of single phase flows the same solver is used but the physical properties are taken as constant and surface tension effects are not present. First, a non-solenoidal velocity field, ${\mathbf{u}^*}_{k+1}$, is computed as

$$\begin{aligned}\frac{\rho_{k+1}^{n+1}\mathbf{u}_{k+1}^{*}-\rho^{n}\mathbf{u}^{n}}{\Delta t} =& -\nabla p_k^{n+1}-\nabla\cdot\left(\rho^{n}{\mathbf{u}_k}^{n+1/2}\left(\frac{\mathbf{u}^{n}+\mathbf{u}_{k+1}^{*}}{2}\right)\right)\\ &+\nabla\cdot\left[\mu^{n+1}\left(\nabla\left(\frac{\mathbf{u}^{n}+\mathbf{u}_{k+1}^{*}}{2}\right)+\nabla\left(\frac{\mathbf{u}^{n}+\mathbf{u}_{k+1}^{*}}{2}\right)\Big|^{T}\right)\right]\\ &+\rho_{k+1}^{n+1}\mathbf{g},\end{aligned} \tag{20}$$

where the intermediate velocity field is

$$\mathbf{u}_k^{n+1/2}=\frac{1}{2}\left(\mathbf{u}_k^{n+1}+\mathbf{u}^{n}\right). \tag{21}$$

Then, a Poisson equation is solved for the pressure increment Φ^{n+1},

$$\nabla \cdot \left(\frac{\Delta t}{\rho_{k+1}^{n+1}} \nabla \left(\Phi^{n+1} \right) \right) = \nabla \cdot \mathbf{u}_{k+1}^{*}. \tag{22}$$

Finally, the velocity and the pressure at the next time step are obtained using Φ^{n+1},

$$\mathbf{u}_{k+1}^{n+1} = \mathbf{u}_{k+1}^{*} - \frac{\Delta t}{\rho_{k+1}^{n+1}} \nabla \left(\Phi^{n+1} \right), \tag{23}$$

$$p_{k+1}^{n+1} = p_{k}^{n+1} + \Phi^{n+1}. \tag{24}$$

Eqs. (20), (22) and (23)-(24) are refered to as *estimation*, *projection*, and *correction*. Δt is the time step size. In the case of multiphase flows, ρ^n and μ^{n+1} values are computed from the old and new VOF field, respectively, whereas ρ_{k+1}^{n+1} is computed in a way that ensures consistency between mass and momentum transport [28]. More details can be found in [33].

At all of these steps, boundary conditions have to be provided: velocity boundary condition after estimation and correction, and pressure boundary condition during projection. At the inflow and on the walls, those steps are straightforward and well documented [34]. For the velocity it simply consists of setting the corresponding values in the velocity vector. As these values will not change during estimation and correction, this step is only necessary after estimation, Eq. (20),

$$\mathbf{u}_{k+1}^{*}\big|_{\partial\Omega_d} = \mathbf{u}_{D}^{n+1}, \tag{25}$$

where $\mathbf{u}_{D}^{n+1}$ is an imposed velocity value given by the physics, i.e., inflow or walls. The definition of the pressure boundary condition is directly obtained from the application of Eq. (23) on those boundaries,

$$\left. \frac{\partial \Phi^{n+1}}{\partial n} \right|_{\partial\Omega_d} = 0. \tag{26}$$

The expression of outlet boundary conditions for velocities and pressure at each step of the projection algorithm, resulting in the application of the OBCs presented in section 2, is detailed in the next subsections.

3.2. Implementation of convective/Neumann OBC

Neumann (NM) and convective (CV) boundary conditions can be directly used to compute outlet velocities at the estimation step. In the CV boundary condition, Eq. (16), a wave velocity c has to be prescribed. In the present work, it is going to be taken as the maximal velocity in the plane just before the exit,

$$c = c_{max} = \max(\mathbf{u}^*_{k+1} \cdot \mathbf{n})_{BC-1}, \tag{27}$$

or as a theoretical wave speed, if available,

$$c = c_{th}. \tag{28}$$

The theoretical expression for the phase velocity will be detailed in the results when used. Except if otherwise stated, the phase velocity will be taken as $c = c_{max}$. What is of interest here is the definition of the pressure boundary condition that will allow to obtain a solution to the Poisson equation, Eq. (22). This comes from the integration of Eq. (22) over the computational domain:

$$\int_{\partial\Omega} \frac{\Delta t}{\rho^{n+1}} \nabla\Phi^{n+1} \cdot \mathbf{n} \mathrm{d}S = \int_{\partial\Omega} \mathbf{u}^*_{k+1} \cdot \mathbf{n} \mathrm{d}S \tag{29}$$

Applying Eq. (26) will directly lead to the following pressure outlet boundary condition,

$$\int_{\partial\Omega} \frac{\Delta t}{\rho^{n+1}} \left.\frac{\partial\Phi^{n+1}}{\partial n}\right|_{\partial\Omega_o} \mathrm{d}S = Q_{in} - Q_{out}, \tag{30}$$

where Q_{in} and Q_{out} are the inlet and outlet flow rates, respectively. Thus, if inlet and outlet flow rates are forced to be the same (including the clipping of negative velocities, as explained in section 2) when considering the application of the velocity OBC and the resolution of the Poisson equation, the pressure outlet boundary condition can simply be a Neumann BC,

$$\left.\frac{\partial\Phi^{n+1}}{\partial n}\right|_{\partial\Omega_o} = 0, \tag{31}$$

thus ensuring that the integral on the left hand side of Eq. (30) is equal to zero. Finally, as the gradient of pressure on all boundaries is equal to zero, there is no need to correct outlet velocities during the correction step. The overall algorithm is presented in algorithm 1.

Input: $\mathbf{u}^n$, p^n, ρ^n in Ω and on $\partial\Omega$
Solve Eq. (17) using VOF advection $\rightarrow \kappa^{n+1}, \mu^{n+1}$ in Ω
for $k = 0$ **to** $k_{max} - 1$ **do**
  Compute ρ_{k+1}^{n+1}
  Solve Eq. (20) $\rightarrow \mathbf{u}_{k+1}^*$ in Ω
  Apply Eq. (25) and Neumann or convective OBC on $\mathbf{u}_{k+1}^*$
  Set all velocities such that $\mathbf{u}_{k+1}^* \cdot \mathbf{n} < 0$ to zero in the outlet section
  Correct outlet flow rate
  Solve Eq. (22) with Eq. (26) and Eq. (31) $\rightarrow \Phi^{n+1}$ in Ω
  Correct velocities Eq. (23) and pressure Eq. (24) $\rightarrow \mathbf{u}_{k+1}^{n+1}$ and p_{k+1}^{n+1} in Ω
end
Output: $\mathbf{u}^{n+1}$, p^{n+1}, ρ^{n+1} in Ω and on $\partial\Omega$

Algorithm 1: Algorithm for Neumann and convective OBCs

3.3. Implementation of traction-free and estimated traction OBC

The implementation of traction boundary conditions in pressure projection methods has been the subject of many publications in recent years [35, 14, 19, 36]. See also [37] in the context of vector penalty method and [38] for an extension to curved artificial boundaries. Note furthermore that all algorithms presented herein may be adapted to velocity correction methods starting from the work presented in [39].

The main difficulty is to ensure the validity of the relation,

$$(-p_{k+1}^{n+1}\mathbf{I} + \mu^{n+1}(\nabla\mathbf{u}_{k+1}^{n+1} + \nabla\mathbf{u}_{k+1}^{n+1^T})) \cdot \mathbf{n} = \mathbf{t}^{n+1} \tag{32}$$

along with the incompressibility constraint at the end of the correction step. The form of the vector $\mathbf{t}^{n+1}$ will depend on the type of traction boundary condition (TF, ET, or CT, see section 2) and will be explained below. A first strategy consists in simply setting the pressure increment to zero at the outlet [14], but this strategy is known to limit the order of convergence of the overall method [36]. An improvement is found whith an update of the outlet pressure through a rotational pressure correction method [17, 18, 19]. It is known with those methods that the use of a rotational pressure correction will significantly improve the convergence order of the overall algorithm. However, in multiphase flows, there is, to our knowledge, only one example of a rotational pressure-correction [20], which involves the resolution of a second linear system due to the absence of an analytical solution for the

pressure increment. Thus, we choose to employ the method presented in [35], extended for multiphase flow and non-zero traction.

The method presented in [35] starts by applying the normal, i.e., perpendicular, projection of the traction boundary condition just after the estimation step, Eq. (20), using the available variables, namely p_k^{n+1} and $\mathbf{u}_{k+1}^*$. To simplify the understanding of the method, the coordinate system is taken to be cartesian (x, y, z) with an artificial boundary oriented along x. This first step is then,

$$-p_k^{n+1} + 2\mu^{n+1}\frac{\partial u_{k+1}^*}{\partial x} = t_x^{n+1}, \tag{33}$$

where t_x^{n+1} is assumed to be known. The final step will be the application of the traction outlet boundary condition on the new variables $\mathbf{u}_{k+1}^{n+1}$ and p_{k+1}^{n+1},

$$-p_{k+1}^{n+1} + 2\mu^{n+1}\frac{\partial u_{k+1}^{n+1}}{\partial x} = t_x^{n+1}. \tag{34}$$

We are then looking for the pressure increment that will ensure the validity of Eq. (34) as well as satisfy the incompressibility condition. We first take the incompressibility condition in the cell just before the boundary,

$$\nabla \cdot \mathbf{u}_{k+1}^{n+1} = \frac{\partial u_{k+1}^{n+1}}{\partial x} + \frac{\partial v_{k+1}^{n+1}}{\partial y} + \frac{\partial w_{k+1}^{n+1}}{\partial z} = 0, \tag{35}$$

where we express $\partial u_{k+1}^{n+1}/\partial x$ using Eq. (33) and Eq. (34), and $\partial v_{k+1}^{n+1}/\partial y$ and $\partial w_{k+1}^{n+1}/\partial z$ using Eq. (23). It leads to

$$\nabla\cdot\mathbf{u}_{k+1}^{n+1} = \frac{p_{k+1}^{n+1} - p_k^{n+1}}{2\mu^{n+1}} + \nabla\cdot\mathbf{u}_{k+1}^* - \frac{\partial}{\partial y}\left(\frac{\Delta t}{\rho_{k+1}^{n+1}}\frac{\partial}{\partial y}\Phi^{n+1}\right) - \frac{\partial}{\partial z}\left(\frac{\Delta t}{\rho_{k+1}^{n+1}}\frac{\partial}{\partial z}\Phi^{n+1}\right). \tag{36}$$

Finally, as the flow is incompressible, the pressure boundary condition is

$$\frac{\partial}{\partial y}\left(\frac{1}{\rho_{k+1}^{n+1}}\frac{\partial}{\partial y}\Phi^{n+1}\right) + \frac{\partial}{\partial z}\left(\frac{1}{\rho_{k+1}^{n+1}}\frac{\partial}{\partial z}\Phi^{n+1}\right) - \frac{1}{2\mu^{n+1}\Delta t}\Phi^{n+1} = \frac{\nabla \cdot \mathbf{u}_{k+1}^*}{\Delta t}, \tag{37}$$

which is the pressure boundary condition derived in [35] adapted to a variable density flow. Previous equations are forming the algorithm used to compute and couple the x-velocity and the pressure at the outflow, and to satisfy exactly the relation Eq. (34) along with the incompressibility constraint. Concerning the tangential components of the velocity, the outflow condition is simply a Neumann condition,

$$\frac{\partial v_{k+1}^{*,n+1}}{\partial x} = \frac{\partial w_{k+1}^{*,n+1}}{\partial x} = 0. \tag{38}$$

This choice, rather than the use of a constraint on the tangential traction value, is motivated by the well-known fact that a tangential traction-free condition is not compatible with a parallel flow [40] and by the fact that several results are reported as better with a Neumann condition on tangential velocities rather than a tangential traction condition, even with non-zero traction [34].

It should be noted that the pressure boundary condition, Eq. (37), is only valid if t_x^{n+1} does not change between the estimation and correction steps. Otherwise, any change will have to be taken into account into the pressure OBC, Eq. (37). Thus, the traction t_x^{n+1} can be given depending on the type of open boundary condition. For TF, it is

$$t_x^{n+1} = \frac{\rho^n}{2} f(\mathbf{u}^n), \tag{39}$$

and for non-zero traction conditions (ET and CT),

$$t_x^{n+1} = \frac{\rho^n}{2} f(\mathbf{u}^n) + t_x^{est,n+1}. \tag{40}$$

The density is taken at the previous time step to be coherent with the choice of the velocity. The backflow stabilization is thus not instantaneous but delayed by one time step. As stated previously, the estimated normal traction is computed using interior values and at the previous iteration to ensure the validity of the pressure boundary condition. For ET,

$$t_x^{est,n+1} = \left(-p + 2\mu \frac{\partial u}{\partial x} \right)_{BC-1}^{n}, \tag{41}$$

and for CT,

$$t_x^{est,n+1} = \phi \left(-p + 2\mu \frac{\partial u}{\partial x} \right)_{BC-1}^{n} + (1-\phi) \left(-p + 2\mu \frac{\partial u}{\partial x} \right)_{BC}^{n}, \tag{42}$$

with ϕ to be prescribed later. The overall algorithm is presented in algorithm 2.

Input: $\mathbf{u}^n$, p^n, ρ^n in Ω and on $\partial\Omega$
Solve Eq. (17) using VOF advection $\rightarrow \kappa^{n+1}, \mu^{n+1}$ in Ω
for $k = 0$ **to** $k_{max} - 1$ **do**
  Compute ρ_{k+1}^{n+1}
  Solve Eq. (20) $\rightarrow \mathbf{u}_{k+1}^{*}$ in Ω
  Apply Eqs. (25)-(33) and (38) on $\mathbf{u}_{k+1}^{*}$
  Solve Eq. (22) with Eq. (26) and Eq. (37) $\rightarrow \Phi^{n+1}$ in Ω
  Correct velocities Eq. (23) and pressure Eq. (24) $\rightarrow \mathbf{u}_{k+1}^{n+1}$ and p_{k+1}^{n+1} in Ω
  Apply Eqs. (34) and (38) on $\mathbf{u}_{k+1}^{n+1}$
end
Output: $\mathbf{u}^{n+1}$, p^{n+1}, ρ^{n+1} in Ω and on $\partial\Omega$

Algorithm 2: Algorithm for traction OBCs

4. Single phase test cases

The improvements obtained using our novel outlet treatment are first illustrated on single phase test cases. The first test case, the Kovasznay flow, allows to see the spatial order of convergence of the overall method, while the second test case, a time-dependent manufactured solution test, allows to study the temporal order of convergence of the present algorithm. The third test case, the flow around a square, shows both qualitative and quantitative improvements thanks to ET. The last case, a turbulent plane jet, shows the stability and accuracy of ET in the presence of a fully turbulent flow.

4.1. Kovasznay flow

The Kovasznay flow is a steady state flow used to mimic the flow behind a cylinder [41]. This configuration is a 2D domain, periodic along the vertical axis, with an inflow on its left boundary and an OBC on its right. The analytical solution of the Kovasznay flow is given by

$$u = 1 - e^{\lambda x}\cos(2\pi y), \tag{43}$$

$$v = \frac{\lambda}{2\pi}e^{\lambda x}\sin(2\pi y), \tag{44}$$

$$p = \frac{1}{2}\left(1 - e^{2\lambda x}\right), \tag{45}$$

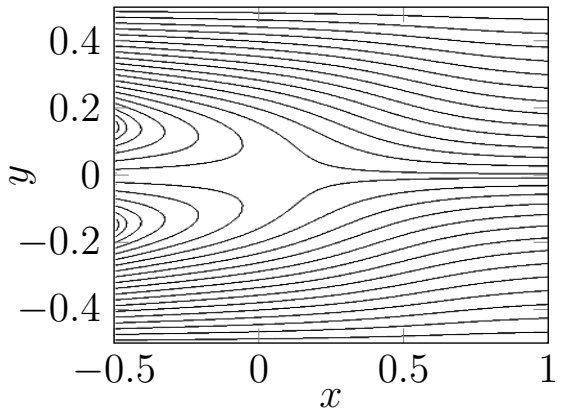

Figure 1: Streamlines of the Kovasznay flow

where $\lambda = \frac{Re}{2} - \sqrt{\frac{Re^2}{4} + 4\pi^2}$. We choose here $Re = 1/40$. Thus, this test case can be used to study the effect of the type of OBC and its position on the error level compared to the analytical solution [17]. The domain is a two-dimensional domain of size $-0.5 \leqslant x \leqslant L_x$ and $-0.5 \leqslant y \leqslant 0.5$, with L_x the position of the OBC. The mesh is uniform and Cartesian with a cell size Δ, with Δ to be specified later. In all cases presented below, $\Delta t = 0.001$. The inflow is defined using the analytical solution in $x = -0.5$. The streamlines of this flow are shown in figure 1.

Hereafter we study the effect of the OBC choice on the error compared to the theoretical solution. Considered OBCs are NM, TF and ET. CV is intentionally excluded from this test case to avoid any discussion on the choice of the convective velocity at this point.

In a first comparative test, the domain length is kept constant with $L_x = 4.5$ and the mesh is progressively refined in order to check the convergence of the error depending on the type of OBC. In figure 2a) we show the evolution of the L_2 error norm of the x-velocity and the pressure, for differents OBCs and depending on mesh resolution. One can first observe two differents behaviors: for coarser meshes, the same level of error is obtained for all three OBCs, which decreases with mesh resolution (with order 2, i.e., the order of used numerical methods). For finer meshes, and for NM and TF OBCs, the error progressively saturates at a constant value, indicating that outflow error is dominating. Note that this deviation occurs later for TF than for NM and stabilizes also at a lower value, meaning that TF gives a lower error than

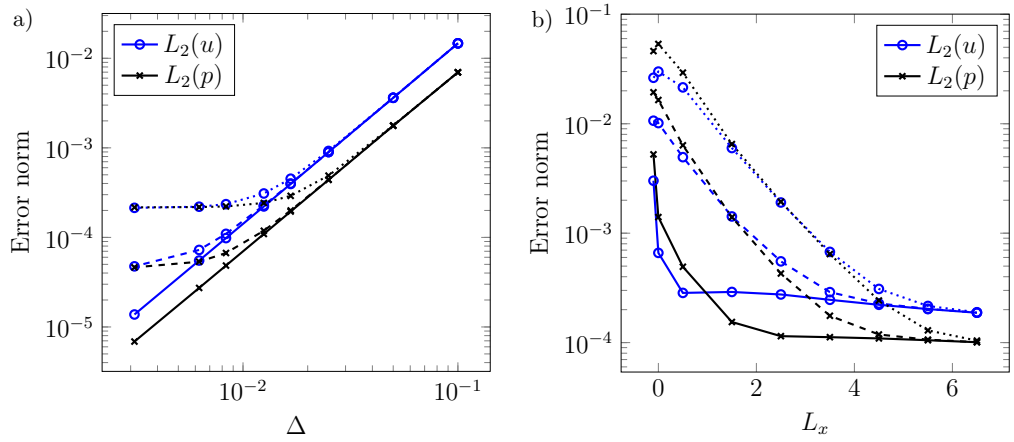

Figure 2: Error levels for different OBCs: a) Mesh convergence, b) Effect of domain truncation. Continuous line: ET - Dashed line: TF - Dotted line: NM

NM on that test case. On the other hand, with ET, no deviation is observed from the second order slope, meaning that in that range of mesh resolutions, the error due to the outflow is never dominating. With finer meshes and ET, one will necessarily observe a saturation of the error as the choice of the estimated traction is not perfect. Note that one can also compute the estimated traction using the analytical solution [17], which is not possible in real flow simulations. Note that second order convergence is also obtained in L_{inf} error norm.

In a second comparative test, the mesh is kept constant ($\Delta = 1/80$) and the domain is progressively truncated. Similarly to the previous test, we show on figure 2b) the evolution of the L_2 error norm of the x-velocity and the pressure, for differents OBCs and depending on the position of the artificial boundary. It is seen in figure 2b) that on a sufficiently long domain all OBCs produce the same level of error. It is also seen that with NM the truncation of the domain has a much stronger effect than with other OBCs. The result is, for the range of L_x considered here and using NM, barely independent of the artifical boundary position. This point is improved with TF, which provides a better independence of the result with the position of the outlet. With ET the result is independent of L_x for a large range of domain size, even though a small increase of $L_2(u)$ is noticeable. Note that all OBCs are stable for the smallest domain ($L_x = -0.1$), where the outflow boundary is located in a recirculation zone, which is not possible without

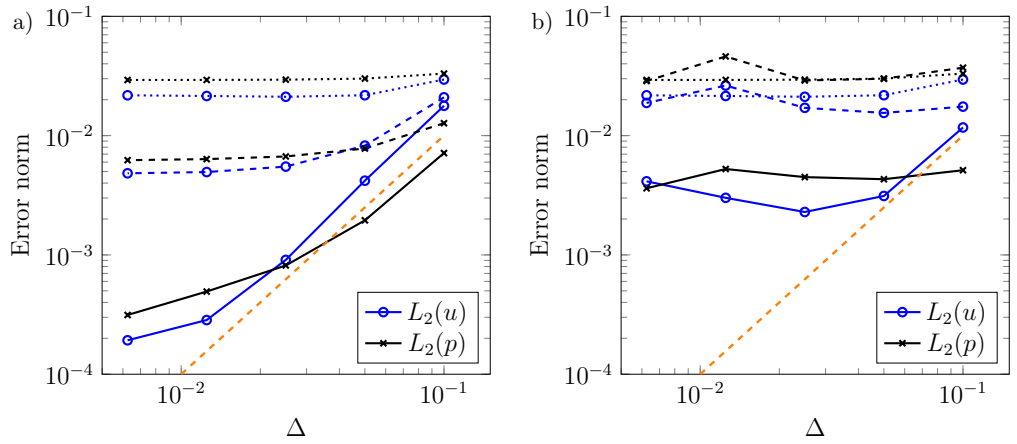

Figure 3: Error levels for different OBCs and two domain lengths: a) $L_x = 0.5$, b) $L_x = -0.1$. Continuous line: ET - Dashed line: TF - Dotted line: NM. The orange dashed line in both plots shows second order spatial convergence.

backflow treatment such as clipping or stabilization. But, in case of the durable presence of a backflow, even the traction condition will not provide a perfectly accurate solution as the stabilization term only makes sense in terms of kinetic energy conservation. In order to examine how the order of spatial convergence is deteriorated whith domain truncation, we show in figure 3, two additional convergence tests with domains shorter than the one used for the test presented in figure 2a). For $L_x = 0.5$, see figure 3a), second order convergence is only obtained for $L_2(u)$ using ET and for a shorter range of resolution than previously. For $L_x = -0.1$, see figure 3b), the outlet boundary is located in the recirculation zone, and no clear convergence of the error with resolution can be observed, even using ET. For all resolutions and domain lengths tested, ET has the lowest level of error. The same results are obtained on L_{inf} error norm.

Those tests demonstrate the interest of the non-zero traction OBC on a steady state problem in terms of error level and independence to outlet position.

4.2. Time-dependent manufactured solution

In order to study the temporal order of convergence of the proposed method, we use the time-dependent manufactured solution of [17],

$$u = 2\cos(\pi y)\sin(\pi x)\sin(t), \tag{46}$$

$$v = -2\cos(\pi x)\sin(\pi y)\sin(t), \tag{47}$$

$$p = 2\sin(\pi x)\sin(\pi y)\cos(t), \tag{48}$$

which satisfies the incompressibility condition ($\nabla \cdot \mathbf{u} = 0$). In order to satisfy Eq. (18), unsteady body forces have to be added to the Navier-Stokes equations.

The computational domain is two-dimensional, of size $0 \leqslant x \leqslant 2$ and $-1 \leqslant y \leqslant 1$, with 256 uniform cells in both directions. Eqs. (46) and (47) are enforced as Dirichlet boundary conditions on three boundaries of the computational domain, whereas the traction condition Eq. (32) is used on the last one. Similarly to [17, 20, 35], the right hand side of Eq. (32) is computed using the manufactured solution. Imposing the analytical traction value at the open boundary is needed to avoid the domination of spatial error over temporal error. No stabilization term is included as it becomes meaningless when one imposes the exact traction at the open boundary, i.e., when the open boundary is transformed into a Dirichlet boundary. The initial velocity field is set to zero, in agreement with the manufactured solution. For this test case we use $\rho = 1$ and $\mu = 0.01$.

The simulation is advanced in time with a fixed time step, Δt, to be specified, until a fixed final time $t_f = 0.5$. The L_2 error norm on different flow variables at this final time is computed with respect to the manufactured solution. The test is then repeated with various time steps.

The results are shown on figure 4. One can see that the error norm convergence for all flow variables is approximately of second order until a progressive saturation of the temporal error by the spatial error. Note that the convergence of the error seems to be faster for the velocities than for the pressure, which may be due to the presence of splitting errors [35]. A rotational pressure correction would be a solution to resolve this discrepancy [35, 17], but for the reason cited in section 3.3 we chose not to use this strategy. Note that the same results are obtained in L_{inf} error norm. In agreement with [35], these results suggest that the present algorithm for the implementation of traction conditions does not deteriorate the order of temporal convergence.

The choice of manufactured solution and computational domain we made involves $\mathbf{u} \cdot \mathbf{n} = 0$ and $p = 0$ at the boundaries (same test case as [17]). In order to prove that the results are not affected by these choices, we use the same manufactured solution on a computational domain shifted along x, i.e.,

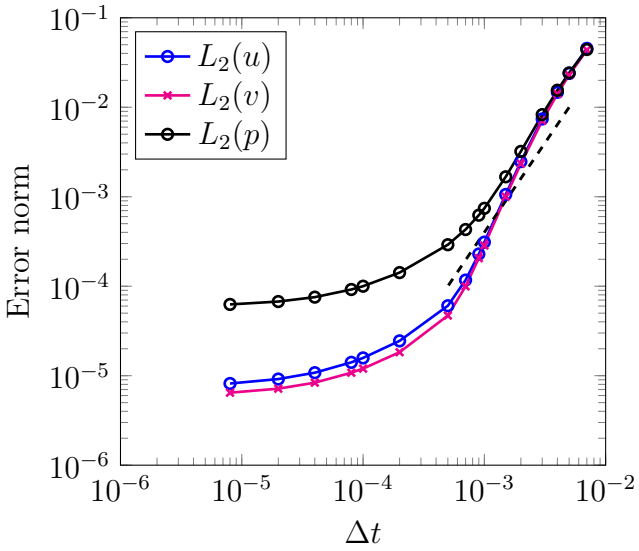

Figure 4: Method of manufactured solution. Convergence of the error level with respect to the time step. The dashed black line shows second order convergence.

with $-0.5 \leqslant x \leqslant 1.5$ and $-1 \leqslant y \leqslant 1$. This way, there is backflow and non-zero pressure at the open boundary at the final time ($t_f = 0.5$). The resolution is the same as previously.

The results are shown in figure 5a). Similarly to the previous results, second order temporal convergence is obtained, though with an error slightly higher than for the previous computational domain. This demonstrates once again that the present algorithm for traction condition does not deteriorate the order of temporal convergence. When we add the stabilization term to the analytical traction value, as done for the results presented in figure 5b), we observe degraded temporal convergence leading to an error plateau. We emphasize that this plateau is fully expected, as the stabilization term is purely ad-hoc and represents a numerical error when added to the analytical traction at the open boundary.

4.3. Flow around a square

We now compare the different OBCs on an unsteady case: the flow over a two-dimensional square. This test case presents two main interests from the point of view of OBC performance. Firstly, we study their ability to convect the vortices generated by the von Kármán instability through the

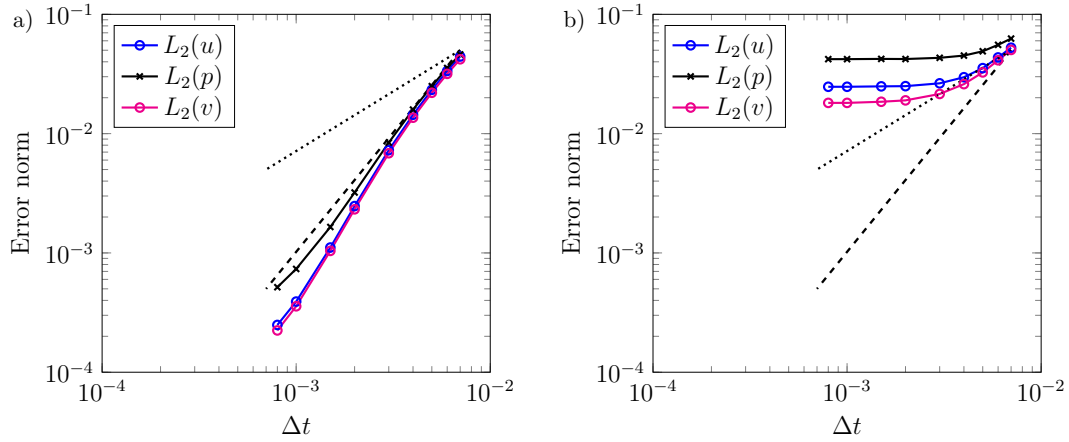

Figure 5: Method of manufactured solution for the shifted domain. Convergence of the error at the final time with respect to the time step, a) imposing the analytical traction at the open boundary, and b) imposing the analytical traction and the stabilization term at the open boundary. The dotted and dashed black lines show first and second order convergence, respectively.

artificial boundary. Secondly, we investigate the impact of the OBC position and type on aerodynamic quantities such as drag and lift coefficients and vortex shedding frequency

In a first test, we use the square as a vortex generator and we compare qualitatively TF and ET on their ability to properly convect vortices through the artificial boundary. The test case is a two dimensional domain of size $-5H \leqslant x \leqslant 5H$ and $-5H \leqslant y \leqslant 5H$ where H is the size of the square located in the middle of the domain. The Reynolds number $Re = \rho U H/\mu$ is equal to 1000. U is the velocity uniformely imposed at the inflow ($x = -5H$) and the outflow is located at $x = 5H$. Symmetry boundary conditions are used at $y = \pm 5H$ and the domain is uniformely discretized with a cell size $\Delta = H/40$. The time step is chosen such that the CFL number stays equal to 1. Under those conditions a strongly unsteady flow is generated downstream of the obstacle. It should be noted that this flow is unphysical given the three-dimensionality of a real flow at that Reynolds number, but this test case allows to assess the accuracy of outlet boundary conditions [17].

On figure 6 we show, through isocontours of z vorticity, the exit of several vortices through the outlet boundary. The top row of figures presents the result with TF, whereas the bottom row of figures presents the result using ET. On the top images, one can observe that the use of TF tends to flatten

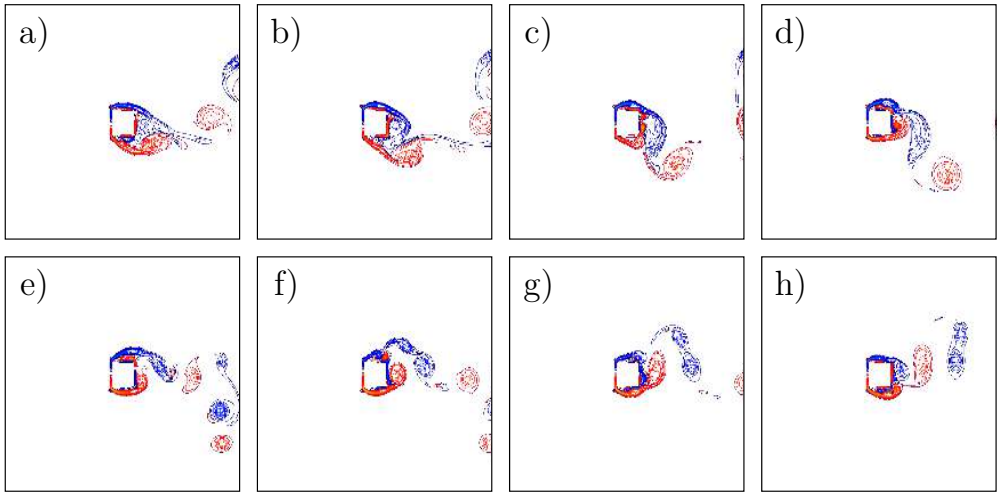

Figure 6: Isocontours of z vorticity. Top figures: TF; bottom figures: ET. From left to right, all figures are separated by a time interval of $0.5H/U$.

the vortices on the outlet and to delay their complete exit through the open boundary. This can simply be explained by a balance of pressure: the pressure at the vortex center is balanced by the imposed outlet pressure through imposed traction and by inertial effects. As inertial effects are not strong enough to push out the vortex, it sticks to the boundary and is only slighty – and slowly – pulled out of the domain by the backflow stabilization term. We observed that if no backflow stabilization is taken into account, vortices were gathering on the artificial boundary, finally leading to the blow-up of the simulation due to the backflow instability. Note that, although the vortices exit seems unnatural, once the stabilization term is included the code remains perfectly stable to backflow at the outlet boundary. On the other hand, with ET, no vortex sticking is observed and vortices simply cross the boundary with barely any deformation.

We now propose a more quantitative comparison between different OBCs through the study of the aerodynamic quantities. To avoid any confinement effect and any impact of the inflow position, the domain is this time of size $-10H \leqslant x \leqslant L$ and $-10H \leqslant y \leqslant 10H$, with L the position of the outlet boundary and H the size of the square located at $(0, 0)$. The Reynolds number $Re = \rho UH/\mu$ is now equal to 100. The domain is discretized with a uniform cell size $\Delta = H/40$ in the sub-domain $-10H \leqslant x \leqslant L$ and

$-4H \leqslant y \leqslant 4H$, to avoid any loss of resolution of the vortices in the wake of the obstacle, and is then progressively stretched up to the top and bottom boundaries with a constant stretching ratio of 1.05. The time step is chosen such that the CFL number stays equal to 1. The aerodynamic forces are directly integrated on the surface of the obstacle.

Figure 7 presents the evolution of differents aerodynamic quantities as a function of the position and the type of open boundary. We also included the results of two recent publications using the stabilized traction-free condition [17] and the traction-free condition [35]. In order to simplify comparison with other publications, the evolution of the aerodynamic quantities is presented in terms of error relative to the value obtained on the longest domain. Figure 7a) shows the evolution of the mean drag coefficient, figure 7b) shows the evolution of the r.m.s lift coefficient and figure 7c) shows the evolution of the Strouhal number associated with the vortex shedding frequency. The results obtained with ET keep a correct behavior even on the smaller domains by exhibiting the lowest variation of aerodynamic quantities as a function of the outflow position. This improvement is largely explained by the fact that the underlying assumption of well-developped flow associated with the traction-free condition, stabilized or not, is no longer required with ET.

4.4. Turbulent plane jet

To finally assess the stability and the accuracy of the proposed boundary condition we study the spatial evolution of a turbulent plane jet. The configuration, the expression of the analytical inlet velocity profile and the choice of parameters are the same as in Da Silva & Metais [42] (case refered to as "DNS2" in their original paper). The numerical domain is a 3D domain of size $0 \leqslant x \leqslant 12.4h$, $-6h \leqslant y \leqslant 6h$ and $-1.6h \leqslant z \leqslant 1.6h$, where h is the jet width. The inlet boundary is located at $x = 0$ and the outflow at $x = 12.4h$. The other boundaries are periodic. The domain is discretized with a uniform cell size $\Delta x = \Delta y = \Delta z = 0.04h$. The constant time step is $\Delta t = 0.02$.

In a first study the Reynolds number based on the jet width, $Re = (U_i - U_{ff})h/\nu$, is taken equal to 3000, with U_i the jet centerline inlet velocity and U_{ff} the inlet far-field velocity. The isocontours of positive Q-criterion [43] are shown on figure 8, using TF (a) and ET (b). On both figures one can see the spatial development of the jet, initiated by the apparition of successive Kelvin-Helmholtz rolls that are then connected by the apparition of vortices in the streamwise direction. When reaching the outlet boundary the flow is fully tridimensional. On figure 8a) one can see the dramatic effect of TF

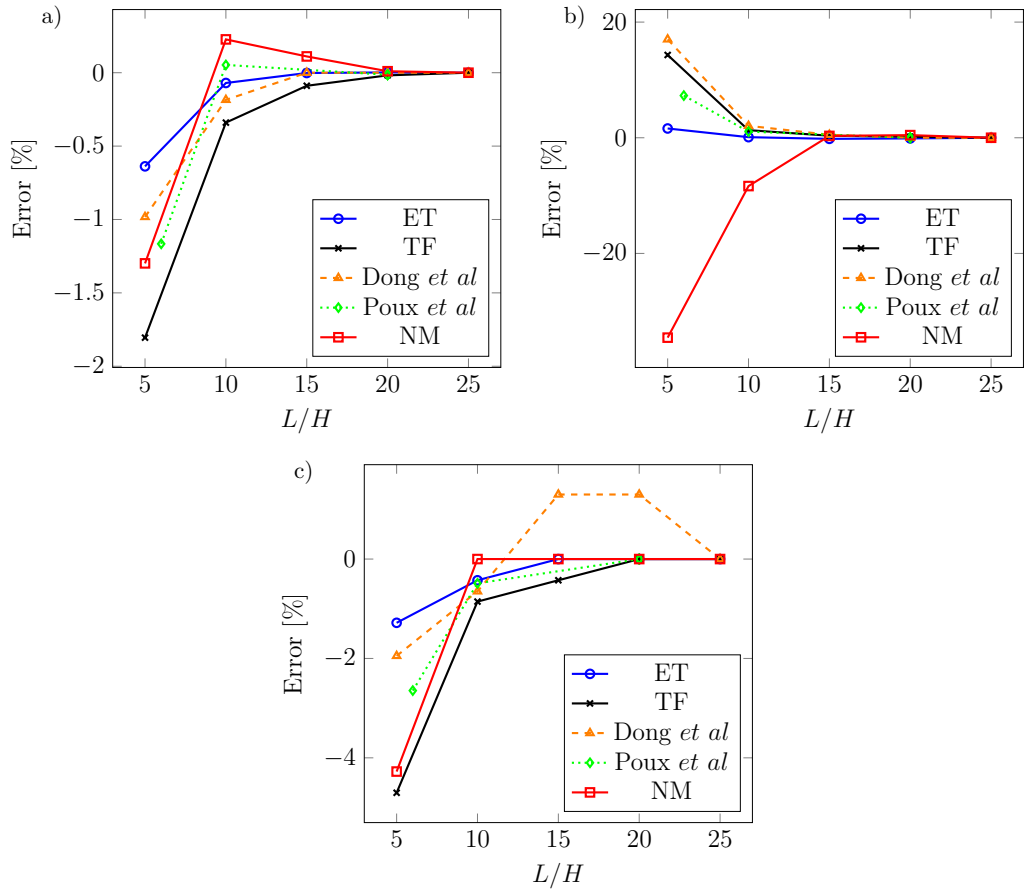

Figure 7: Impact of the outflow position and type on the aerodynamic quantities: a) mean drag coefficient, b) r.m.s lift coefficient, c) Strouhal number. On all plots, the vertical axis is the error compared to the value obtained on the longest domain, whereas the horizontal axis is the distance between the square and the outflow position L normalized by the size of the square H. The reference results included are the results from Dong *et al* [17] and Poux *et al* [35].

on the exit of the vortices. A part of them sticks to the boundary and is prevented to leave the domain. On the other hand, using ET, no vortex sticking is observed and the vortices are crossing the boundary with barely any deformations, see figure 8b). With CV, the vortices exit looks very similar to the one seen using ET (results not shown). Note that using TF we had to reduce the time step size in order to obtain a stable simulation. This may be due to the vortex sticking phenomena coupled to the delayed backflow correction of one time step. Considering the poor qualitative result seen on figure 8a) and the need to decrease the time step size, we therefore exclude TF from the following analysis.

The jet exhibits a self-similar behaviour in its downstream region [42]. In this region, several quantities computed from the time averaged velocity field are evolving linearly with the downstream distance. We choose here to use the centerline velocity, $U_c = \langle u(x, y = 0)\rangle$, and the jet half-width, $\delta_{1/2}$, defined as the $y-$location where the velocity is equal to half of the centerline velocity, i.e., $\langle u(x, y = \delta_{1/2})\rangle - U_{x,\infty} = 0.5\,(U_c - U_{x,\infty})$, with $U_{x,\infty} = \langle u(x, y = \infty)\rangle$, the far-field velocity. Those quantities follow the following relationships [44]:

$$\frac{\delta_{1/2}}{h} = K_{u1}\left[\frac{x}{h} + K_{u2}\right], \tag{49}$$

and

$$\left[\frac{U_i - U_{ff}}{U_c - U_{x,\infty}}\right]^2 = C_{u1}\left[\frac{x}{h} + C_{u2}\right]. \tag{50}$$

We plot those quantities, along with their linear relations, on figure 8c) and 8d) using ET and CV. Using ET, in addition to provide a natural exit of the vortices as well as the stability of the simulation, the self-similar region is barely disturbed by the presence of the open boundary. With CV both of the self-similar quantities are strongly affected by the presence of the outflow. Note that the slopes of the linear relations are the same as in Da Silva & Metais [42].

To demonstrate that the proposed boundary treatment is stable for highly turbulent flows, we study the large eddy simulation of the turbulent plane jet at $Re = 30000$. The sub-grid stresses are estimated with a dynamic Smagorinsky eddy viscosity model using Lagrangian averaging to compute the dynamic coefficient [45]. The computational domain is now larger in the vertical direction to account for the entrainment induced by the jet, i.e., $-8h \leqslant y \leqslant 8h$. The isocontours of positive Q-criterion are shown on

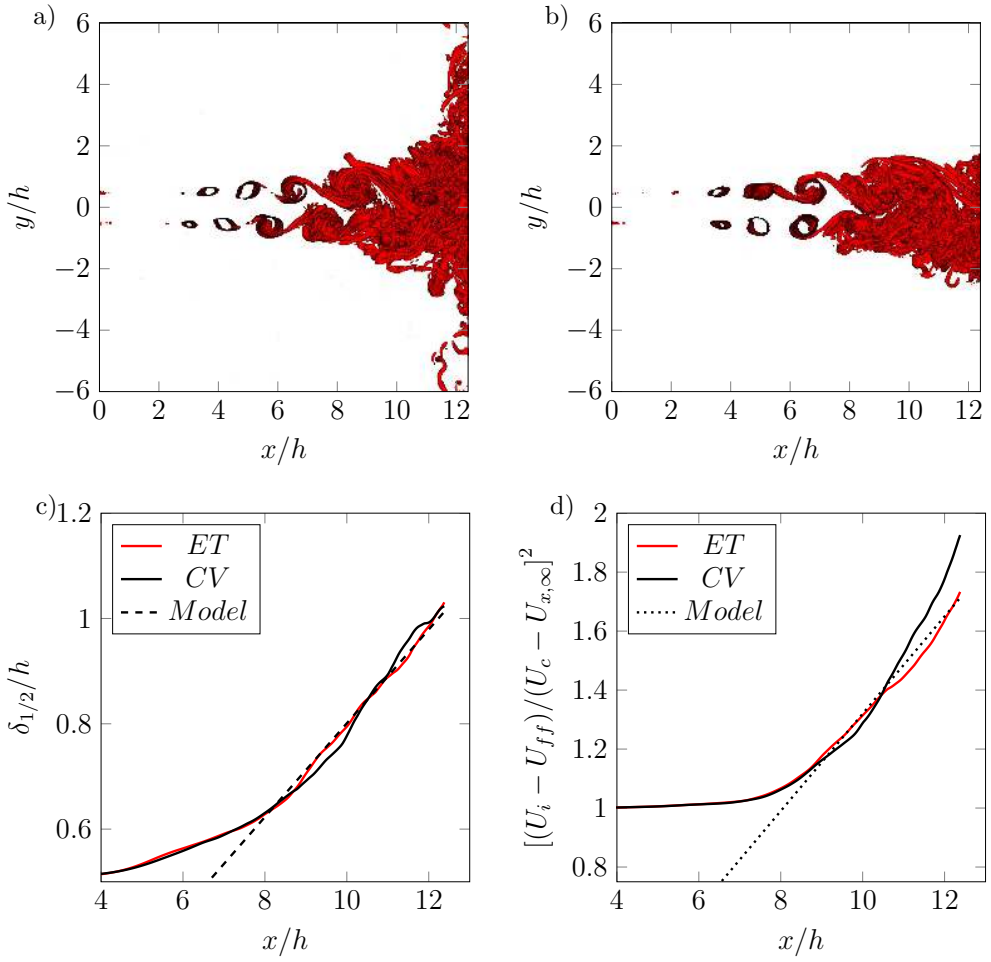

Figure 8: (Color online) Turbulent plane jet at $Re = 3000$. Positive Q-criterion isocontours (20 isocontours from $Q = 0.25$ to $Q = 100$) at $t(U_i - U_{ff})/h = 166$, using TF (a) and ET (b). c) Evolution of the jet half-width with downstream distance using ET and CV. Model computed using Eq. (49) with $K_{u1} = 0.089$ and $K_{u2} = -1$. d) Evolution of the centerline jet velocity with downstream distance using ET and CV. Model computed using Eq. (50) with $C_{u1} = 0.165$ and $C_{u2} = -2$.

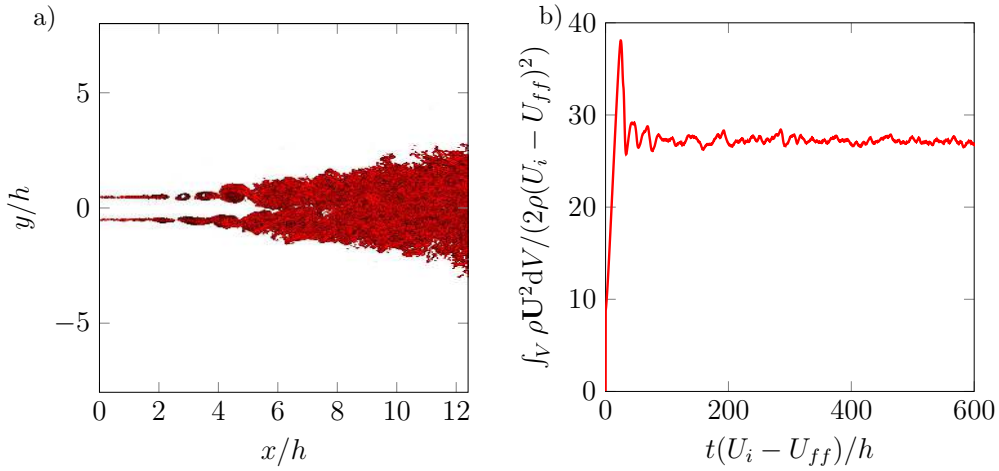

Figure 9: Large eddy simulation of a turbulent plane jet at $Re = 30000$. a) Positive Q-criterion isocontours (10 isocontours from $Q = 0.25$ to $Q = 100$) at $t(U_i - U_{ff})/h = 400$ using ET. b) Temporal evolution of the normalized kinetic energy integrated over the domain using ET.

figure 9a). One can see that there is no accumulation of vortices on the open boundary although the turbulence is fully developped when reaching the open boundary. To show the long-term stability of the proposed method even in the presence of a strong turbulent flow, we show the temporal evolution of the kinetic energy integrated over the computational domain on figure 9b). After an initial transient, the flow reaches a statistically stationary state that is not perturbed by the presence of backflow at the open boundary. As stated before, this result strongly suggests that a zero energy flux at the open boundary is not needed to ensure the stability of the simulation. The accuracy of the proposed boundary treatment could even be improved using a better estimation of the traction at the open boundary, for example with CT.

5. Multiphase test cases

We now turn our attention to multiphase flows. In this section, the importance of backflow stabilization is demonstrated using first a single drop advection test case, then a turbulent swirling jet flow simulation. Finally, we demonstrate the improvements obtained using CT on a problem of surface waves reflection.

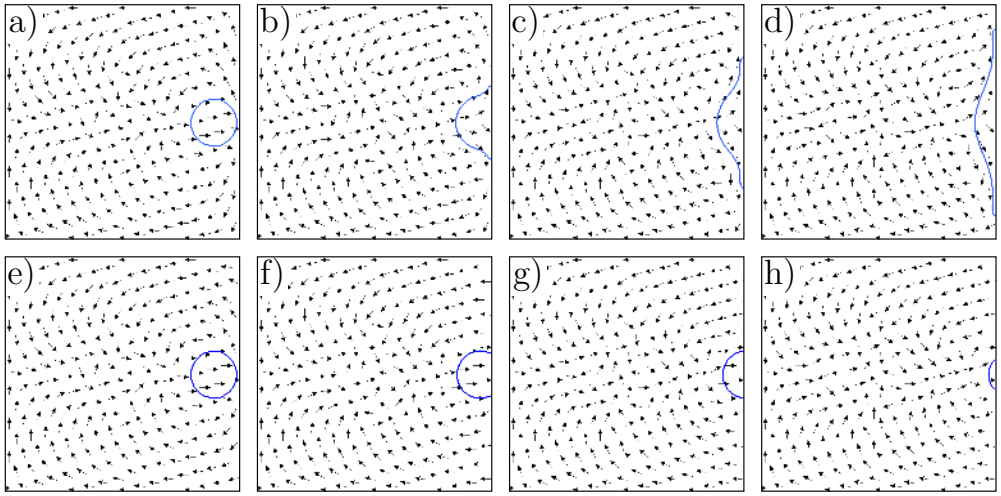

Figure 10: Water drop advection in a domain without inlet. a)-d) : CV ; e)-h) : ET. From left to right, all figures are separated by a time interval of $0.6D/U_l$.

5.1. Drop convection

A water droplet of size $D = 0.1$ with initial velocity $U_l = 3$ is placed at the center a domain of size $-10D \leqslant x \leqslant 10D$ and $-10D \leqslant y \leqslant 10D$ and surrounded by quiescent air. The outflow is located at $x = 10D$, with periodic boundary conditions at $y = \pm 10D$. At $x = -10D$, a slip wall condition is used. The simulation is run on a 64×64 mesh with a timestep $\Delta t = 0.001$.

Figure 10 shows velocity vectors along with the liquid-gas interface during the advection of the drop towards the outlet for two types of boundary conditions. On the top row of images the result are obtain with the CV, and on the bottom row of images the result are obtained with ET. Note that, on this test case, one can replace CV by NM and ET by TF, for the same qualitative result.

On the top pictures of figure 10, one can observe that with CV OBC the drop is flattening on the boundary and no liquid is exiting the domain. On the other hand, using ET, the drop is completely going out with minimal deformation. The reason for these completely different behaviors lies in the fact that the incompressibility condition requires the outlet flow rate to be equal to the inlet flow rate, in this case zero. Thus, the only way for the drop to exit is to allow backflow. We see here one strong limitation of the clipping

strategy, which severely affects the flow by preventing the drop from going out, though it provides unconditional stability. On the other hand, once the stabilization term is included, ET and TF are perfectly stable to backflow as can be seen in figures 10f-g-h).

5.2. Turbulent swirling jet

To show the importance of backflow stabilization in a more realistic case, we present a simulation of turbulent swirling jet. As shown in figure 11, a turbulent liquid jet exits from a nozzle located on the left of the domain. The jet then develops into a conical shape and becomes subject to different interfacial instabilities leading to its atomization. The outflow is located on the right of the domain (colored in pink), whereas all lateral boundary conditions are periodic. All physical properties, injection parameters and geometric characteristics are the same as in [46]. The domain is discretized with a $200 \times 400 \times 400$ cartesian grid and the simulation is advanced with a CFL number of 0.8.

On figures 11a) and 11b), the liquid-gas interface colored by the axial velocity is shown after a simulation time $tU/D = 11$, where U is the bulk injection velocity, and D the external diameter of the injector. On figure 11a), the result with CV is shown, with the phase velocity computed using Eq. (27). One can see that since this outflow treatment does not allow backflow, some of the liquid is prevented from going out and "splashes" on the exit plane. Figure 11b) shows the result using the ET OBC, and in this case the liquid is not blocked on the exit plane. This obviously has a large impact on the capability to reach long term simulations of such atomizing liquid jets. With a boundary condition that does not allow backflow, the simulation time is obvisouly limited by the length of the domain, which is not the case with a stabilized traction boundary condition. It should be noted here that CV may be replaced by NM and ET by TF for the same results on the liquid exit. The difference between TF and ET will lie in the speed of the droplets in the vicinity of the outlet and in the behavior of the vortices exiting the domain, as already discussed using the test case of the flow around a square.

Although here traction conditions are used only as exit conditions, it should be noted that they may also be used as lateral boundary condition [21, 47]. One can also imagine replacing the wall used around the liquid injector by an open traction boundary condition in order to get a more realistic

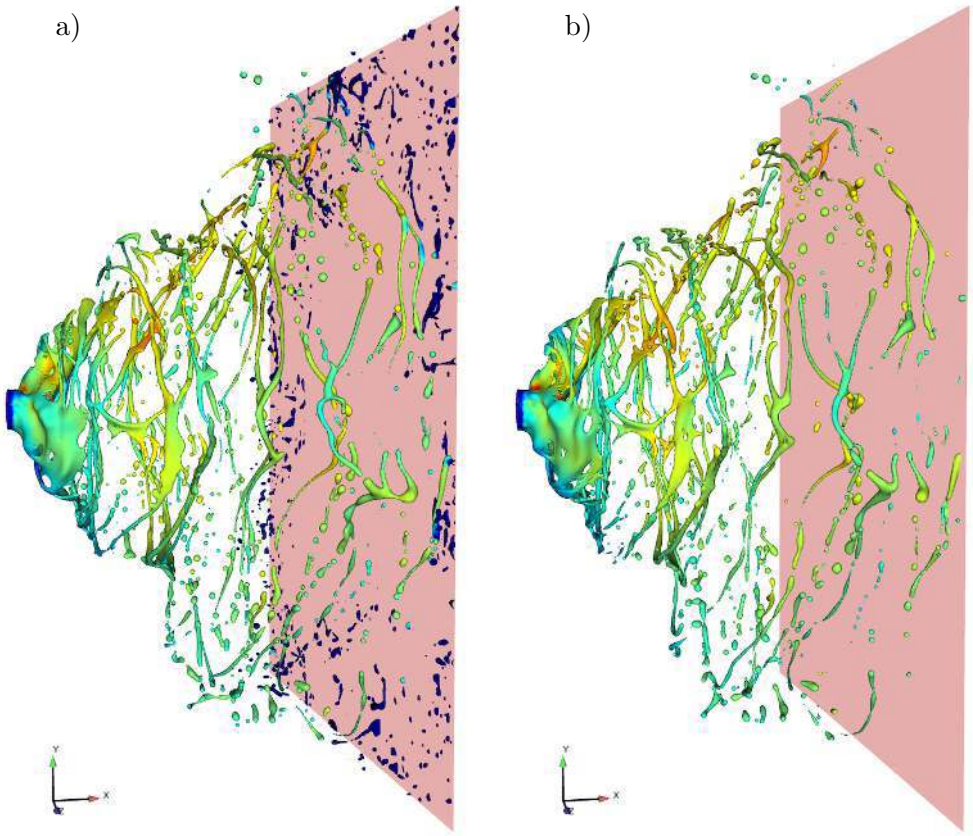

Figure 11: (Color online) Turbulent swirling jet test case. Liquid-gas interface colored by axial velocity shown at a time $tU/D = 11$ (dark blue: $u = 0$, dark red: $u = 3U$, with U the bulk injection velocity). a) result using CV, b) result using ET.

representation of such jets by allowing the development of a "natural" gas co-flow. We will investigate that point in future works.

5.3. Surface gravity waves

We finally evaluate the ability of the different OBCs to evacuate a surface wave without reflection. As said in the introduction, wave reflection is a problem of critical importance in ocean modeling as it prevents the convergence of flow statistics and may create unrealistic flows [4].

The test case is set up using solitary wave theory [48]. The interface

height is defined as

$$\eta(x) = A_0 \text{sech}^2 \left(\sqrt{\frac{3A_0}{4{h_0}^3}} x \right), \tag{51}$$

with A_0 the initial height of the wave and h_0 the water depth. The initial velocity is defined as $\mathbf{u} = (u(x), 0, 0)$ where

$$u(x) = \eta(x) \frac{\sqrt{|g| \left(h_0 + A_0\right)}}{h_0 + \eta(x)} + U_{in}, \tag{52}$$

and U_{in} is the inflow velocity. The computational domain is two-dimensional, of size $-60h_0 \leqslant x \leqslant 20h_0$ and $-h_0 \leqslant y \leqslant 4h_0$ with symmetry boundary conditions along y, a constant velocity inflow $u = U_{in}$ at $x = -60h_0$ and the OBC at $x = 20h_0$. Air/water conditions are used for the choice of physical properties. This setup results in the transport of a soliton from the position $x = 0$ to the OBC at a constant phase velocity $c_{th} = \sqrt{|g| \left(h_0 + A_0\right)} + U_{in}$. For all cases presented below parameters are chosen as $A_0 = 0.005$, $h_0 = 0.01$, $U_{in} = 0.07$. The domain is discretized using a uniform Cartesian mesh with $\Delta x = \Delta y = 5 \times 10^{-4}$. The solution is advanced using a time step size $\Delta t = 1 \times 10^{-3}$.

On figure 12 are presented the space-time plots of the interface height for 4 different OBCs along with, on figure 13, the interface height signals at a position $x = 10h_0$. On figure 12a), the result with CV is shown. As in previous tests, the wave speed is taken as $c = c_{max}$. One can first see a transient phenomenon at the initialization which causes the emission of perturbations towards the left of the domain and the height of the wave to slightly decrease. Since the inflow is located at $x = -60h_0$, none of the results presented herein are affected by the reflexion of these initial perturbations on the inflow. The reason for these perturbations is an initial adjustment due to the discrete approximations of the continuous solution [4]. Following this initial transient, the soliton travels towards the OBC at a constant speed c_{th}. Once the wave reaches the artificial boundary, it completely crashes on the boundary and a large part is reflected in the domain in a succession of smaller waves, forming a reflection cone. This result is not a surprise given the inapropriate choice of the convective velocity.

In figure 12c), we use the theoretical wave speed as the convective velocity in CV. One can see that the reflection is much lower in amplitude but creates

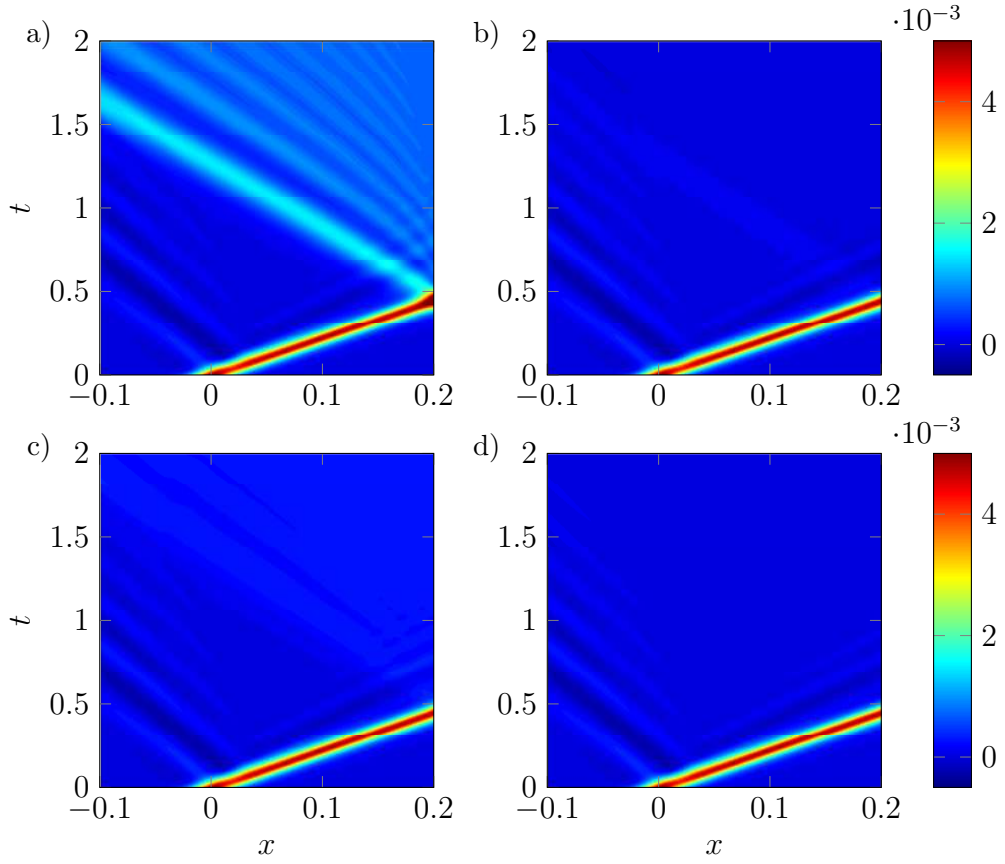

Figure 12: (Color online) Transport of a surface gravity waves through an OBC. a) CV with $c = c_{max}$, b) ET, c) CV with $c = c_{th}$, d) CT with $c = c_{th}$. The color indicates the liquid height.

an increase of the mean liquid level, seen also in figure 13. Thus, even with the best choice of the wave speed, a convective condition is not able to evacuate a soliton out of the domain without reflection.

We now focus our study on the use of a traction condition. First, it should be noted that the use of TF is impractical for such simulations. The pressure being hydrostatic in the domain, using a traction-free condition will impose a pressure close to zero at the outlet (velocity gradients being small far from the soliton), thus resulting in a strong suction of the flow which rapidly propagates up to the inlet. On figure 12b), we show the result using the ET. One can observe that the reflection is almost suppressed but that small

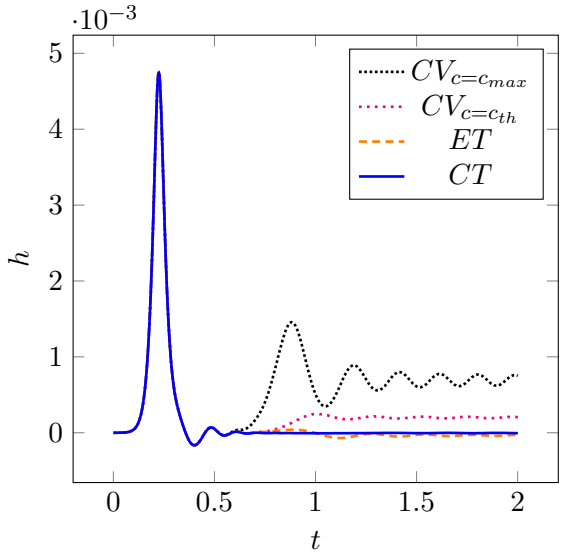

Figure 13: Interface height signals at a fixed position $x = 10h_0$ for 4 different OBCs.

waves propagate upstream. Thus, such an arbitrary choice of the estimated traction (computed at the point just before the boundary at the previous time step) is in fact even better than the best choice of a convective OBC. However, two points have to be emphasized. Firstly, ET is not perfectly non-reflective. Secondly, we have observed a dependence of its performance to numerical parameters such as the time step or cell sizes.

The reason for the last two points has in fact already been explained in section 2. Considering the estimated traction as a Lagrangian quantity, the present choice is not optimal. Indeed, taking the estimation of the traction at the point before the boundary and at the previous time step is not always a good choice depending on numerical parameters. A more accurate choice can be found considering the convected traction boundary condition (CT). The theoretical wave speed, c_{th}, is taken as the advection velocity. The interpolation coeficient used in Eq. (14) is therefore $\phi = c_{th}\Delta t/\Delta x$. The result using this approach is shown on figures 12d) and 13).

One can see that CT, our new OBC, is now perfectly non-reflective. It must be emphasized that this result is now independent of the time step, the mesh size, and is also independent of the OBC position.

5.4. Additional remark

In most of the present paper, we use an estimation of the traction at the point just before the boundary, which is easy to define on a structured mesh. The extension to fully unstructured meshes is possible thanks to the Lagrangian estimation of the traction introduced previously, as done in Eq. (14). On such meshes, one has to define an advection velocity and then perform a semi-Lagrangian interpolation of the traction field at the location of interest to obtain the traction estimate. In case of curved boundaries, one has to use differential geometry to complete the pressure boundary condition, Eq. (37), as done in [38].

6. Conclusion

We have presented a comparison between several outlet boundary treatments on single and multiphase test cases along with their numerical implementation in the context of fractional step methods. One major difference between these open boundary conditions lies in the backflow treatment. The implementation of backflow clipping associated with Neumann or convective open boundary conditions, while providing unconditional stability, can have a strong effect in the simulation of multiphase flows. On the other hand, stabilized traction conditions are perfectly suited to resolve this issue. The main drawback of the traction-free condition lies in its underlying assumption of well-developed flow that is not suited for severely truncated domains or high Reynolds number flows. To overcome this issue, an open boundary condition combining stabilization to backflow and space and time varying estimated traction is proposed, allowing stable and accurate simulations for turbulent and multiphase flows. This estimated traction is considered as a Lagrangian quantity, which allows to use it as a non-reflective artifical boundary for surface waves simulations. This work shows that traction conditions have the potential to resolve most of issues related to outflow treatment. They might also be used as lateral or inlet boundary conditions and allow a considerable reduction in the cost of numerical simulations, as we will explore in future work. The very general form under which the estimated traction is introduced also opens the way to a study of the effect of different advection methods on the accuracy of traction boundary conditions.

Acknowledgements

We acknowledge Prof. Eric Blayo, for pointing to our attention the work of [16] and for several discussions, as well as Dr. Alexandre Poux and Prof. Mahdi Esmaily for fruitful discussions. This work was sponsored by the Office of Naval Research (ONR) as part of the Multidisciplinary University Research Initiatives (MURI) Program, under grant number N00014-16-1-2617, and by the IDEX UGA "International Strategic Partnerships" program. A part of the simulations were performed using HPC resources from GENCI-CINES (Grant No. A0072A00611).

References

[1] E. Blayo, L. Debreu, Revisiting open boundary conditions from the point of view of characteristic variables, Ocean Modelling 9 (3) (2005) 231–252.

[2] R. L. Sani, P. M. Gresho, Resumé and remarks on the open boundary condition minisymposium, International Journal for Numerical Methods in Fluids 18 (10) (1994) 983–1008.

[3] C. Bertoglio, A. Caiazzo, Y. Bazilevs, M. Braack, M. Esmaily, V. Gravemeier, A. L. Marsden, O. Pironneau, I. E. Vignon-Clementel, W. A. Wall, Benchmark problems for numerical treatment of backflow at open boundaries, International Journal for Numerical Methods in Biomedical Engineering 34 (2) (2018) e2918.

[4] P. Marchesiello, J. C. McWilliams, A. Shchepetkin, Open boundary conditions for long-term integration of regional oceanic models, Ocean Modelling 3 (1-2) (2001) 1–20.

[5] M. E. Moghadam, Y. Bazilevs, T.-Y. Hsia, I. E. Vignon-Clementel, A. L. Marsden, et al., A comparison of outlet boundary treatments for prevention of backflow divergence with relevance to blood flow simulations, Computational Mechanics 48 (3) (2011) 277–291.

[6] H. Persillon, M. Braza, Physical analysis of the transition to turbulence in the wake of a circular cylinder by three-dimensional Navier-Stokes simulation, Journal of Fluid Mechanics 365 (1998) 23–88.

[7] I. Orlanski, A simple boundary condition for unbounded hyperbolic flows, Journal of Computational Physics 21 (3) (1976) 251–269.

[8] D. R. Durran, Open boundary conditions: fact and fiction, in: IUTAM Symposium on Advances in Mathematical Modelling of Atmosphere and Ocean Dynamics, Springer, 2001, pp. 1–18.

[9] W. H. Raymond, H. Kuo, A radiation boundary condition for multi-dimensional flows, Quarterly Journal of the Royal Meteorological Society 110 (464) (1984) 535–551.

[10] R. L. Higdon, Radiation boundary conditions for dispersive waves, SIAM Journal on Numerical Analysis 31 (1) (1994) 64–100.

[11] B. Engquist, A. Majda, Absorbing boundary conditions for numerical simulation of waves, Proceedings of the National Academy of Sciences 74 (5) (1977) 1765–1766.

[12] G. Jin, M. Braza, A nonreflecting outlet boundary condition for incompressible unsteady Navier-Stokes calculations, Journal of Computational Physics 107 (2) (1993) 239–253.

[13] C. Taylor, J. Rance, J. Medwell, A note on the imposition of traction boundary conditions when using the FEM for solving incompressible flow problems, Communications in Applied Numerical Methods 1 (3) (1985) 113–121.

[14] J. Liu, Open and traction boundary conditions for the incompressible Navier–Stokes equations, Journal of Computational Physics 228 (19) (2009) 7250–7267.

[15] N. Hasan, S. F. Anwer, S. Sanghi, On the outflow boundary condition for external incompressible flows: A new approach, Journal of Computational Physics 206 (2) (2005) 661–683.

[16] C.-H. Bruneau, P. Fabrie, Effective downstream boundary conditions for incompressible Navier-Stokes equations, International Journal for Numerical Methods in Fluids 19 (8) (1994) 693–705.

[17] S. Dong, G. E. Karniadakis, C. Chryssostomidis, A robust and accurate outflow boundary condition for incompressible flow simulations

on severely-truncated unbounded domains, Journal of Computational Physics 261 (2014) 83–105.

[18] S. Dong, An outflow boundary condition and algorithm for incompressible two-phase flows with phase field approach, Journal of Computational Physics 266 (2014) 47–73.

[19] S. Dong, J. Shen, A pressure correction scheme for generalized form of energy-stable open boundary conditions for incompressible flows, Journal of Computational Physics 291 (2015) 254–278.

[20] S. Dong, X. Wang, A rotational pressure-correction scheme for incompressible two-phase flows with open boundaries, PloS one 11 (5) (2016) e0154565.

[21] S. Dong, A convective-like energy-stable open boundary condition for simulations of incompressible flows, Journal of Computational Physics 302 (2015) 300–328.

[22] C.-H. Bruneau, Boundary conditions on artificial frontiers for incompressible and compressible navier-stokes equations, ESAIM: Mathematical Modelling and Numerical Analysis 34 (2) (2000) 303–314.

[23] C.-H. Bruneau, P. Fabrie, New efficient boundary conditions for incompressible navier-stokes equations: a well-posedness result, ESAIM: Mathematical Modelling and Numerical Analysis 30 (7) (1996) 815–840.

[24] A. Clément, Coupling of two absorbing boundary conditions for 2D time-domain simulations of free surface gravity waves, Journal of Computational Physics 126 (1) (1996) 139–151.

[25] M. Owkes, O. Desjardins, A computational framework for conservative, three-dimensional, unsplit, geometric transport with application to the volume-of-fluid (VOF) method, Journal of Computational Physics 270 (2014) 587–612.

[26] G. Tryggvason, R. Scardovelli, S. Zaleski, Direct numerical simulations of gas–liquid multiphase flows, Cambridge University Press, 2011.

[27] O. Desjardins, G. Blanquart, G. Balarac, H. Pitsch, High order conservative finite difference scheme for variable density low Mach number

turbulent flows, Journal of Computational Physics 227 (15) (2008) 7125–7159.

[28] J. Palmore Jr, O. Desjardins, A volume of fluid framework for interface-resolved simulations of vaporizing liquid-gas flows, Journal of Computational Physics 399 (2019) 108954.

[29] M. Kang, R. P. Fedkiw, X.-D. Liu, A boundary condition capturing method for multiphase incompressible flow, Journal of Scientific Computing 15 (3) (2000) 323–360.

[30] E. Marchandise, P. Geuzaine, N. Chevaugeon, J.-F. Remacle, A stabilized finite element method using a discontinuous level set approach for the computation of bubble dynamics, Journal of Computational Physics 225 (1) (2007) 949–974.

[31] K. Goda, A multistep technique with implicit difference schemes for calculating two or three-dimensional cavity flows, Journal of computational physics 30 (1) (1979) 76–95.

[32] S. A. Teukolsky, Stability of the iterated Crank-Nicholson method in numerical relativity, Physical Review D 61 (8) (2000) 087501.

[33] O. Desjardins, J. McCaslin, M. Owkes, P. Brady, Direct numerical and large-eddy simulation of primary atomization in complex geometries, Atomization and Sprays 23 (11).

[34] P. M. Gresho, Incompressible fluid dynamics: some fundamental formulation issues, Annual Review of Fluid Mechanics 23 (1) (1991) 413–453.

[35] A. Poux, S. Glockner, M. Azaïez, Improvements on open and traction boundary conditions for Navier-Stokes time-splitting methods, Journal of Computational Physics 230 (10) (2011) 4011–4027.

[36] J.-L. Guermond, P. Minev, J. Shen, Error analysis of pressure-correction schemes for the time-dependent Stokes equations with open boundary conditions, SIAM Journal on Numerical Analysis 43 (1) (2005) 239–258.

[37] P. Angot, R. Cheaytou, Vector penalty-projection method for incompressible fluid flows with open boundary conditions, in: Proceedings of Algoritmy, 2012, pp. 219–229.

[38] E. Bänsch, A finite element pressure correction scheme for the Navier-Stokes equations with traction boundary condition, Computer Methods in Applied Mechanics and Engineering 279 (2014) 198–211.

[39] A. Poux, S. Glockner, E. Ahusborde, M. Azaïez, Open boundary conditions for the velocity-correction scheme of the Navier-Stokes equations, Computers & Fluids 70 (2012) 29–43.

[40] J. M. Leone Jr, P. M. Gresho, Finite element simulations of steady, two-dimensional, viscous incompressible flow over a step, Journal of computational physics 41 (1) (1981) 167–191.

[41] L. Kovasznay, Laminar flow behind a two-dimensional grid, in: Mathematical Proceedings of the Cambridge Philosophical Society, Vol. 44, Cambridge University Press, 1948, pp. 58–62.

[42] C. B. da Silva, O. Métais, On the influence of coherent structures upon interscale interactions in turbulent plane jets, Journal of Fluid Mechanics 473 (2002) 103–145.

[43] Y. Dubief, F. Delcayre, On coherent-vortex identification in turbulence, Journal of turbulence 1 (1) (2000) 011–011.

[44] E. Gutmark, I. Wygnanski, The planar turbulent jet, Journal of Fluid Mechanics 73 (3) (1976) 465–495.

[45] C. Meneveau, T. S. Lund, W. H. Cabot, A lagrangian dynamic subgrid-scale model of turbulence, Journal of fluid mechanics 319 (1996) 353–385.

[46] F. Evrard, F. Denner, B. van Wachem, A multi-scale approach to simulate atomization processes, International Journal of Multiphase Flow 119 (2019) 194–216.

[47] C.-H. Bruneau, S. Tancogne, Far field boundary conditions for incompressible flows computation, Journal of Applied Analysis and Computation 8 (3) (2018) 690–709.

[48] W. H. Munk, The solitary wave theory and its application to surf problems, Annals of the New York Academy of Sciences 51 (3) (1949) 376–424.